Enhancing high frequency sensitivity of gravitational wave detectors with a Sagnac interferometer

Teng Zhang,* Denis Martynov, and Haixing Miao†

School of Physics and Astronomy, and Institute for Gravitational Wave Astronomy, University of Birmingham, Edgbaston, Birmingham B15 2TT, United Kingdom

Stefan Danilishin

Department of Gravitational Waves and Fundamental Physics, Maastricht University, P.O. Box 616, 6200 MD Maastricht, The Netherlands and Nikhef, Science Park 105, 1098 XG Amsterdam, The Netherlands

(Received 1 October 2021; accepted 23 November 2021; published 20 December 2021)

The sensitivity of gravitational-wave detectors is limited in the high-frequency band by quantum shot noise and eventually limited by the optical loss in the signal recycling cavity. This limit is the main obstacle to detecting gravitational waves from binary neutron star mergers in the current and future-generation detectors, as it does not depend on either the arm length in the high-frequency band or the injected squeezing level. In this paper, we present the sloshing-Sagnac interferometer topology, which can be obtained from the Michelson interferometer by optically connecting the end mirrors into an additional optical cavity. This transforms the interferometer into a triply coupled cavity system capable of beating the loss-induced high-frequency limit of the signal-recycled Michelson interferometer. With the upgrade plan of Advanced LIGO, A+ comparable parameters, a sloshing-Sagnac scheme can achieve 7 times better sensitivity at 2.5 kHz or a 4 times better signal-to-noise ratio for a typical waveform of binary neutron star post merge. Being an evolution of a Michelson interferometer, the sloshing-Sagnac interferometer can possibly be used as a topology for the future-generation detectors and upgrades of current detectors.

DOI: 10.1103/PhysRevD.104.122003

I. INTRODUCTION

On August 17, 2017, the network of the LIGO and Virgo gravitational-wave (GW) detectors observed gravitational waves from a binary neutron star inspiral for the first time [1]. This observation, apart from being an unprecedented scientific breakthrough in its own right, was the first multimessenger observation of a collision of neutron stars in both the electromagnetic and gravitational-wave spectra [2], which also revealed the origin of heavy chemical elements in the Universe [3]. Additionally, it produced a handful of exciting scientific outcomes, such as a new test of general relativity [4], a novel way to measure the Hubble constant [5,6], and a potential mechanism for generating short gamma-ray bursts [7].

The tidal effect of the mergers of binary neutron stars imprinted on gravitational waves starts to dominate from 500 Hz onwards. The post-merger signatures are seen in the gravitational-wave signal starting from 1 kHz. The eventual post-merger remnant may be a long-lived neutron star or a black hole from collapse [8–11]. However, the post-merger phase of a gravitational-wave signal remains undetected due to insufficient sensitivity of GW detectors at higher frequencies. It is crucial, however, to measure this phase in order to understand the formation of the remnant star and reveal the equation of state of nuclear matter [12–14]. The dominant noise in gravitational-wave detectors above 1 kHz is quantum shot noise, and the sensitivity is eventually limited by the vacuum fields originating from optical loss in the signal recycling cavity (SRC).

Quantum shot noise can be attributed to the vacuum fluctuations of the electromagnetic wave's amplitude and phase that stem from the fundamental uncertainty relation between energy and time, $\Delta E \Delta t \geq \frac{\hbar}{2}$. In the minimum-uncertainty state, it defines the best achievable quantum-noise-limited sensitivity, known as the quantum Cramér-Rao bound (QCRB) [15], which is also called as energetic or fundamental quantum limit [16,17] in the field of gravitational-wave instrument science. The power spectral density corresponding to this limit for a Fabry-Perot-Michelson interferometer reads [18,19]

$$S_{\mathrm{QCRB}}(\Omega) = \frac{c^2\hbar^2}{2S_{PP}(\Omega)L_{\mathrm{arm}}^2}, \tag{1}$$

*tzhang@star.sr.bham.ac.uk
†haixing@star.sr.bham.ac.uk

where S_{PP} is the spectral density of power fluctuations of light in the arms, and $L_{\rm arm}$ is the arm length. As follows from this formula, one can reduce the QCRB by increasing the intracavity power or by injecting the phase-squeezed vacuum fields into the readout port of the interferometer (i.e., amplifying the fluctuations of the amplitude quadrature).

In real life detectors, however, the QCRB is not a practical bound. The decoherence due to optical loss sets the actual limit. The loss adds extra quantum noise on top of the inherent vacuum fluctuations, and sets a new bound on the sensitivity of GW detectors. By its nature, the quantum limit pertaining to loss is a limit to how much squeezing—or, more generally, quantum coherence—the intracavity light can possibly sustain, thereby setting a margin of usefulness of the noise cancellation schemes such as squeezing. Therefore, the only way to improve the signal-to-noise ratio of the measurement apparatus beyond the loss limit is through enhancing its response to the signal.

As demonstrated in Ref. [19], for a Fabry-Perot-Michelson interferometer it is the optical loss in a signal recycling cavity that dominates the quantum noise contribution at frequencies higher than 1 kHz due to the finite bandwidth of the interferometer response. There are several ways to improve the high-frequency signal response of the signal-recycled interferometer, e.g., by using the SRC-arm coupled cavity resonance [8,20,21], detuning the SRC [22], implementing active white-light cavities [23–25], or using a nonlinear optical parametric amplifier inside the SRC, known as a "quantum expander" [26]. However, the SRC loss limit, being an internal loss of the coupled SRC-arm cavity system, is solely determined by the optical features of the arm cavity. Any quantum scheme that does not enhance the signal before it decays from the arm cavity is thus marginally helpful. At frequencies beyond the arm cavity bandwidth (∼100 Hz for LIGO interferometers), the power spectral density of SRC loss reads

$$S_{\rm loss}^{\rm HF}(\Omega) = \frac{\hbar\Omega^2}{\omega_0 P_{\rm arm} T_{\rm ITM}} \epsilon_{\rm SRC}, \tag{2}$$

where $\epsilon_{\rm SRC}$ is the round-trip loss in the SRC, ω_0 is the laser wavelength, $P_{\rm arm}$ is the arm cavity circulating power, and $T_{\rm ITM}$ is the power transmissivity of the input test mass (ITM), which determines the power ratio between the input and arms. The SRC loss-limited sensitivity at high frequencies is independent of the length of the arms.

Optical resonance within arms at high frequencies can be achieved by detuning the arm cavities [27]. However, the required detuning is so high that it leads to significant loss of circulating power and to the strong attenuation of one of the signal sidebands, thereby reducing the signal response. In this paper, we propose to use an additional sloshing cavity formed by the end test masses of the folded Fabry-Perot-Michelson interferometer to create a high-frequency resonance response. This configuration is similar to the sloshing-Sagnac interferometer of Refs. [28,29] with a reduced number of test masses, which greatly improves the controllability of the interferometer. The additional sloshing cavity can be tuned so as to enhance the high-frequency signal within arms and thereupon go beyond the SRC loss-limited sensitivity of a Fabry-Perot-Michelson interferometer.

This paper is organized as follows. In Sec. II we describe the characteristics of the sloshing-Sagnac interferometer. In Sec. III we describe the quantum limit from optical losses of the sloshing-Sagnac interferometer. In Sec. IV we describe the impact of interferometer asymmetry and show the sensitivity of the interferometer.

II. GENERAL DESCRIPTION OF THE SLOSHING-SAGNAC INTERFEROMETER

The key idea of our scheme is to enhance the high-frequency signal before it decays from the arms by means of creating an additional optical resonance at high frequency. To achieve this goal, we transform the interferometer into an effective triply coupled cavity. We couple the two arms by optically connecting the end test mass (ETM), as shown in Fig. 1. The new cavity formed by the two ETMs is called the sloshing cavity (SC). The triply

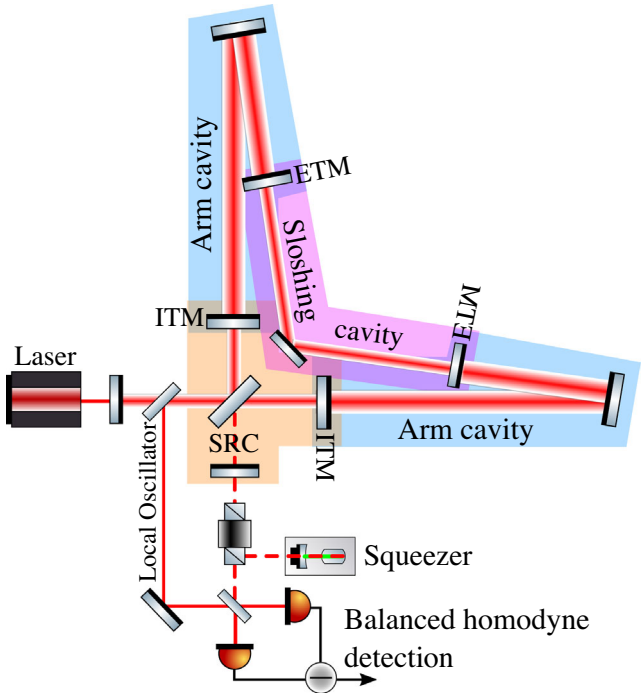

FIG. 1. Schematic of dual recycled sloshing-Sagnac interferometer. The 6 km arm cavity is folded within a 4 km vacuum infrastructure. Two ETMs form a 4 km sloshing cavity. The signal is detected with balanced homodyne readout. This high-frequency configuration is shot-noise limited in the whole frequency band and only requires constant phase quadrature squeezing.

coupled cavity system formed by the SC and the arms can be shown to have three normal modes, with the central one at the carrier frequency ω_0 and the two modes symmetrically split around the central one by the so-called sloshing frequency ω_s. The sloshing frequency and bandwidth of each mode are given by [8,30–32]

$$\omega_s = \frac{c\sqrt{T_{\rm ETM}}}{\sqrt{2L_{\rm arm}L_c}}, \qquad \gamma = \frac{cT_{\rm ITM}}{4L_{\rm arm}}, \tag{3}$$

where $T_{\rm ETM}$ is the power transmissivity of the ETM and L_c is the length of the sloshing cavity. Note that the effective bandwidth of the interferometer with the signal recycling cavity is $\frac{cT_{\rm SRC}}{4L_{\rm arm}}$, where $T_{\rm SRC} = \frac{T_{\rm ITM}T_{\rm SRM}}{[1-\sqrt{(1-T_{\rm ITM})(1-T_{\rm SRM})}]^2}$ is the effective transmissivity of the SRC, when it is operated in the so called *resonant sideband extraction* mode [33]. $T_{\rm SRM}$ is the signal recycling mirror transmissivity. The transmissivities of each arm's ITM and ETM are assumed to be equal to the corresponding transmissivities of the other arm's mirrors.

The propagation of light fields through the interferometer is as follows: (1) laser beams from the main beam splitter travel through three cavities in the clockwise and counterclockwise directions and recombine at the beam splitter, akin to a Sagnac interferometer; (2) the two counterpropagating waves build up power in all cavities constructively; (3) the power in each arm cavity is $\frac{2}{T_{\rm ITM}}$ times the laser power at the beam splitter, which is the same as for a Fabry-Perot-Michelson interferometer; 4) the power in the sloshing cavity is $\frac{(-1+\sqrt{1-T_{\rm ETM}})^2(1+\sqrt{1-T_{\rm ITM}})^2}{2T_{\rm ITM}T_{\rm ETM}}$ times that in the beam splitter.

III. LOSS-LIMITED SENSITIVITY

In the single-mode approximation, the power spectral density of arm loss is calculated as

$$S_{\rm loss}^{\rm arm} = \frac{\hbar c^2}{4\omega_0 L_{\rm arm}^2 P_{\rm arm}}\epsilon_{\rm arm}, \tag{4}$$

where $\epsilon_{\rm arm}$ is the round trip loss in each arm cavity. The power spectral density of arm loss is the same as that of a Michelson interferometer, since the arm loss, since the additional vacuum from arm loss mixes with signal directly in both cases. Considering a 100 ppm loss, the arm loss is not the dominant effect in the detector sensitivity.

The power spectral density of SRC loss of the sloshing-Sagnac interferometer can be calculated as

$$S_{\rm loss}^{\rm SRC}(\Omega) = S_{\rm shot}(\Omega)\epsilon_{\rm SRC}, \tag{5}$$

where $\sqrt{S_{\rm shot}}$ is the shot-noise-limited sensitivity of the sloshing-Sagnac interferometer without the SRC:

$$\sqrt{S_{\rm shot}(\Omega)} = \left|\frac{(\gamma\Omega - i\Omega^2 + i\omega_s^2)}{\sqrt{T_{\rm ITM}}\Omega}\sqrt{\frac{\hbar}{\omega_0 P_{\rm arm}}}\right|. \tag{6}$$

Compared with the noise from the SRC loss of a Michelson interferometer in Eq. (2), when $\Omega = \omega_s$, the SRC loss-limited sensitivity of a sloshing-Sagnac interferometer is improved by a factor of

$$\sqrt{\frac{S_{\rm loss}^{\rm HF}(\omega_s)}{S_{\rm loss}^{\rm SRC}(\omega_s)}} = \frac{\omega_s}{\gamma}. \tag{7}$$

Here, ω_s (which is around 2.5 kHz $\times 2\pi$ in this paper) is much larger than the arm cavity bandwidth γ (which is around 40 Hz $\times 2\pi$ for Advanced LIGO).

The sensitivity of the sloshing-Sagnac interferometer is actually limited by the new loss from the SC, and its power spectral density is calculated as

$$S_{\rm loss}^{\rm SC} = \frac{\hbar\omega_s^4}{2\omega_0 P_{\rm arm}T_{\rm ETM}\Omega^2}\epsilon_{\rm SC}, \tag{8}$$

where $\epsilon_{\rm SC}$ is the round trip loss in the SC. Compared with Eq. (2), at $\Omega = \omega_s$, the loss-limited sensitivity of the new scheme can be improved by a factor of

$$\sqrt{\frac{S_{\rm loss}^{\rm HF}(\omega_s)}{S_{\rm loss}^{\rm SC}(\omega_s)}} = \sqrt{\frac{T_{\rm ETM}\epsilon_{\rm SC}}{2T_{\rm ITM}\epsilon_{\rm SRC}}}. \tag{9}$$

Note that the sensitivity limit stemming from losses in either the SRC or SC is independent of the arm length in the single-mode approximation.

As described in Ref. [8], the main contribution to the SRC loss comes from the wavefront distortion at the ITMs due to the thermal lensing effect. The effective SRC loss in the differential mode is only half of the total loss in both ITMs. The effective SC loss, however, is defined as the total loss from both ETMs. If we assume that $T_{\rm ITM} = T_{\rm ETM}$ and $\epsilon_{\rm SC} = 2\epsilon_{\rm SRC}$, then the SC loss-limited sensitivity of the sloshing-Sagnac interferometer is equal to that of a signal-recycled Fabry-Perot-Michelson interferometer at ω_s. One can also conclude that better sensitivity can be achieved at higher values of $T_{\rm ETM}$. Taking the Advanced LIGO parameters, we show the improvement of the loss-limited sensitivity provided by the sloshing-Sagnac scheme as the shaded area in Fig. 2. Here $T_{\rm ETM}$ is chosen to be equal to 0.12. The circulating power in the SC is 4.5 times that of the laser power at the beam splitter. Other parameters are shown in Table I.

IV. INTERFEROMETER ASYMMETRY

The Sagnac interferometer is highly sensitive to the symmetry of the arms and the beam splitter [34]; however, the influence of asymmetries, such as the skewed

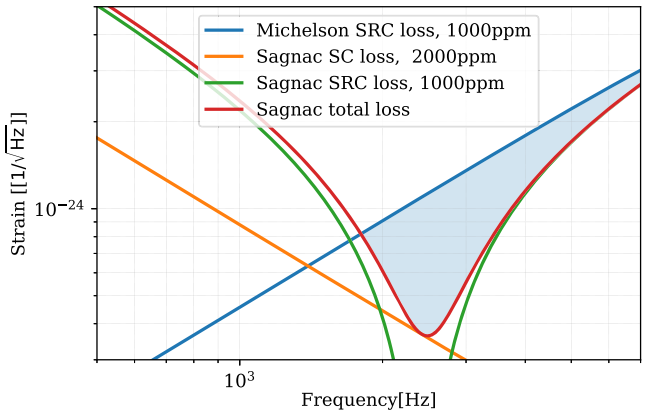

FIG. 2. Loss-limited sensitivity of a sloshing-Sagnac interferometer with arm power 800 kW. The red line represents the sensitivity limit from total loss, which is formed by the SRC loss (red) and SC loss (green). The blue area denotes the improvement of the sensitivity limit from a Michelson interferometer to a sloshing-Sagnac interferometer. The parameters used are listed in Table I.

beam-splitter ratio and impedance mismatch between the ITMs/ETMs in the two arms, is mainly limits the sensitivity where radiation pressure noise dominates. In the shot-noise-limited high-frequency detector and the frequency band of interest (>1 kHz), the influence on the detector response is negligible as long as the arm power is kept at the design level.

In our design, we implement a balanced homodyne readout. For the phase quadrature measurement, the photocurrent of the general balanced homodyne readout can be written as [35]

$$I = L\hat{o}_s - O\hat{l}_s, \tag{10}$$

TABLE I. Parameters of the interferometer.

Wavelength	1064 nm
Mirror mass	40 kg
Arm length	6 km (folded)
SC length	4 km
Arm circulating power	800 kW/4 MW
Sloshing cavity power	25 kW/125 kW
Local oscillator power/Signal port power	20
ITM transmittivity	0.014
ETM transmittivity	0.12
SRM transmittivity	0.2
Input squeezing level	15 dB
Observed squeezing level (2.5 kHz)	6 dB
Arm loss	100 ppm
SRC loss	1000 ppm
SC loss	2000 ppm
Input loss	5%
Output loss	10%

where L is the local oscillator amplitude, O is the light amplitude at the signal port, $\hat{o}_s$ is the phase fluctuation at the signal port including both noise and gravitational-wave signal, and $\hat{l}_s$ is the local oscillator phase noise. Due to asymmetry, the laser stationary component and noise fluctuations will couple to the interferometer signal port. At the same time, the squeezed vacuum from the dark port gets lost to the laser port. However, a calculation shows that the coupling factor between the laser port and the readout port is so tiny that the corresponding loss effect can be ignored. For example, the coupling from the laser port to the readout port due to beam-splitter imbalance is $|R_{\mathrm{BS}} - T_{\mathrm{BS}}|^2$, where R_{BS} and T_{BS} are the beam-splitter power reflectivity and transmissivity, respectively. However, the absolute power that appears at the signal port after the signal-recycling mirror is important. In addition, note that the signal-recycling cavity will further amplify the power of light that couples through the beam splitter by $\sim 4/T_{\mathrm{SRM}}$. To maintain a good signal-to-noise ratio, the second term in Eq. (10) needs to be much smaller than the first term, i.e., $L \gg O$, as usual. With only the asymmetry effect taken into account, the observed noise level is $\frac{|O|^2}{|L|^2} + e^{-2r}$, where $e^{-2r} = 0.1$ means 10 dB squeezing. We simulate the dark port leaking power by using simulation software, FINESSE [36]. Assuming 0.1% asymmetry between two ITMs/ETMs and between the transmissivity and reflectivity of the beam splitter, the resulting leaking power at the signal port is ~20 mW. The asymmetry is defined as the difference over the average of two values. In this case, implementing a 400 mW local oscillator with only the asymmetry effect taken into account, the observed noise level under 15 dB injection squeezing is expected to be 10.8 dB. For 1% asymmetry, the leaking power at signal port will be ~2 W. It could lead large number of photodetectors for bearing the high power of the signal beam. One solution is to split the high-frequency signal sidebands and DC light with a so-called amplitude filter cavity [37] at the interferometer output. The amplitude filter cavity is an impedance matched cavity and with bandwidth much smaller than ω_s. Hereby, the low-frequency filed will transmit through the filter cavity and the high-frequency sidebands will be reflected from the filter cavity. This additional filter scheme could almost eliminate the impact of asymmetry. In this work, we assume the local oscillator power is a factor of 20 of the signal beam power. It corresponds to 0.1% asymmetry without including amplitude filter cavity. The orange line in the lower panel of Fig. 3 shows ~10.8 dB observed squeezing considering asymmetries. Including losses, the observed squeezing is shown as the green line in the lower panel of Fig. 3. The results are carried out by using software, FINESSE and the parameters are listed in Table I. The sensitivity of the detector is shot-noise limited in the whole frequency band, and the peak sensitivity is a factor of 7 better than the design sensitivity of the upgrade

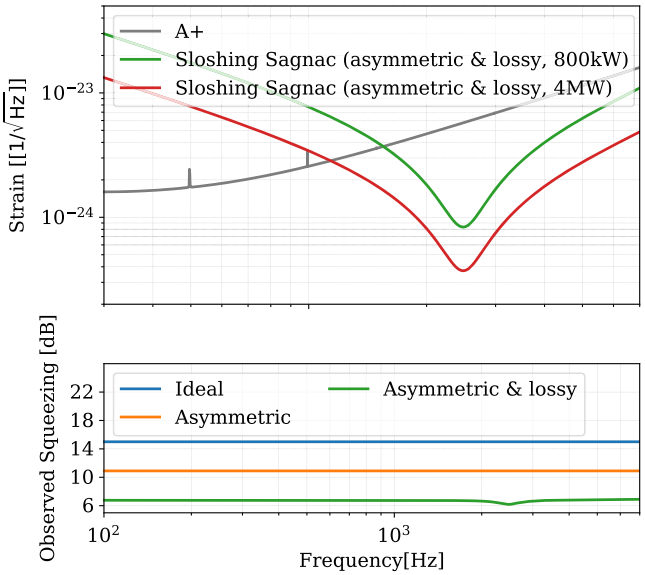

FIG. 3. Upper panel: sensitivity of a sloshing-Sagnac interferometer with different circulating power in the arms. The grey line is the design sensitivity of the upgrade plan of Advanced LIGO, A+. The green and red lines are the corresponding sensitivities of the sloshing-Sagnac interferometer with arm power 800 kW and 4 MW, respectively. The parameters are listed in Table I. Lower panel: observed squeezing of a 800 kW interferometer in different cases with 15 dB injection squeezing. The blue line is the ideal case, while the orange line indicates the impact caused by asymmetries when the ratio of the local oscillator power and the beam power at the signal port is 20. The green line includes both asymmetries and losses.

plan of Advanced LIGO, A+, at $\omega_s \approx 2.5\text{kHz} \times 2\pi$ [38]. We take the typical waveform of binary neutron star post merge in Ref. [9] as the signal model, the resulting signal-to-noise ratio is a factor 4 better than that of A+. An example of 4 MW arm power is also shown in Fig. 3, as a comparison to a high frequency detector design called LIGO-HF in Ref. [39]. Note that, with 4 MW in the arm cavity, the SC power is 125 kW. Thus, the power that goes through the ETM substrates is increased by a factor of 5 of that in the configuration with 800 kW arm cavity power. In order to keep the SC loss on the same level, around 5 times better suppression of the effect of thermal lenses is required [8,40].

V. CONCLUSION AND DISCUSSION

In this paper we introduced a new type of interferometer—the sloshing-Sagnac interferometer—that is able to that is able to achieve better sensitivity than the SRC loss sensitivity limit of a Michelson interferometer. This relies on the enhanced signal response at resonant mode of triply coupled cavities. Meanwhile, the new induced internal loss—the SC loss—can be mitigated by lowering the finesse of the sloshing cavity. In the interferometer, the macroscopic cavity lengths need to be determined to fulfill the required resonant frequency. Two 6 km arm cavities and a 4 km sloshing cavity can possibly be folded into a 4 km facility, which is the same as LIGO facility. Assuming the same beam size as that of a 4 km configuration with straight arms, the folded configuration gives similar mirror thermal noise [41].

As an outlook, the sloshing-Sagnac interferometer studied in this paper is also a speed meter. A speed-meter-type low-frequency response following Ω can be observed in Fig. 3. Exploiting a different part of the parameter space, i.e., lower ω_s, the low-frequency signal will be enhanced and the sensitivity will be limited by radiation pressure noise. Compared with a Michelson interferometer, a speed meter has lower radiation pressure noise. Therefore, this type of sloshing-Sagnac interferometer can also serve as a broadband low-frequency detector.

ACKNOWLEDGMENTS

We thank the support from simulation software, FINESSE. We thank Lee McCuller, Jan Harms, Yanbei Chen, and Mikhail Korobko for fruitful discussion. T. Z., D. M., and H. M. acknowledge the support of the Institute for Gravitational Wave Astronomy at the University of Birmingham, the Science and Technology Facilities Council (STFC), Quantum Technology for Fundamental Physics program (Grant No. ST/T006609/1), and the Engineering and Physical Sciences Research Council (EPSRC), New Horizons program (Grant No. EP/V048872/1). Haixing Miao is supported by a UK STFC Ernest Rutherford Fellowship (Grant No. ST/M005844/11). Stefan Danilishin acknowledges the support of the Faculty of Science and Engineering of Maastricht University.

[1] B. P. Abbott, R. Abbott, T. D. Abbott *et al.* (LIGO Scientific and Virgo Collaborations), GW170817: Observation of Gravitational Waves from a Binary Neutron Star Inspiral, Phys. Rev. Lett. **119**, 161101 (2017).

[2] B. P. Abbott, R. Abbott, T. D. Abbott, F. Acernese, K. Ackley, C. Adams, T. Adams, P. Addesso, R. X. Adhikari, V. B. Adya *et al.*, Multi-messenger observations of a binary neutron star merger, Astrophys. J. Lett. **848**, L12 (2017).

[3] D. Kasen, B. Metzger, J. Barnes, E. Quataert, and E. Ramirez-Ruiz, Origin of the heavy elements in binary neutron-star mergers from a gravitational-wave event, Nature (London) **551**, 80 (2017).

[4] B. P. Abbott, R. Abbott, T. Abbott, F. Acernese, K. Ackley, C. Adams, T. Adams, P. Addesso, R. Adhikari, V. Adya *et al.*, Gravitational waves and gamma-rays from a binary neutron star merger: GW170817 and GRB 170817A, Astrophys. J. Lett. **848**, L13 (2017).

[5] T. L. S. and T. V. Collaborations, A gravitational-wave standard siren measurement of the hubble constant, Nature (London) **551**, 85 (2017).

[6] K. Hotokezaka, E. Nakar, O. Gottlieb, S. Nissanke, K. Masuda, G. Hallinan, K. P. Mooley, and A. T. Deller, A hubble constant measurement from superluminal motion of the jet in GW170817, Nat. Astron. **3**, 940 (2019).

[7] B. P. Abbott, R. Abbott, T. D. Abbott, F. Acernese, K. Ackley, C. Adams, T. Adams, P. Addesso, R. X. Adhikari, V. B. Adya *et al.*, Gravitational waves and gamma-rays from a binary neutron star merger: GW170817 and GRB 170817A, Astrophys. J. Lett. **848**, L13 (2017).

[8] D. Martynov, H. Miao, H. Yang, F. H. Vivanco, E. Thrane, R. Smith, P. Lasky, W. E. East, R. Adhikari, A. Bauswein, A. Brooks, Y. Chen, T. Corbitt, A. Freise, H. Grote, Y. Levin, C. Zhao, and A. Vecchio, Exploring the sensitivity of gravitational wave detectors to neutron star physics, Phys. Rev. D **99**, 102004 (2019).

[9] T. Zhang, J. c. v. Smetana, Y. Chen, J. Bentley, D. Martynov, H. Miao, W. E. East, and H. Yang, Toward observing neutron star collapse with gravitational wave detectors, Phys. Rev. D **103**, 044063 (2021).

[10] P. J. Easter, P. D. Lasky, and A. R. Casey, Can we measure the collapse time of a post-merger remnant for a future gw170817-like event?, arXiv:2106.04064.

[11] N. Sarin and P. D. Lasky, The evolution of binary neutron star post-merger remnants: A review, Gen. Relativ. Gravit. **53**, 59 (2021).

[12] A. Bauswein, H.-T. Janka, K. Hebeler, and A. Schwenk, Equation-of-state dependence of the gravitational-wave signal from the ring-down phase of neutron-star mergers, Phys. Rev. D **86**, 063001 (2012).

[13] K. Takami, L. Rezzolla, and L. Baiotti, Constraining the Equation of State of Neutron Stars from Binary Mergers, Phys. Rev. Lett. **113**, 091104 (2014).

[14] A. Bauswein and N. Stergioulas, Unified picture of the post-merger dynamics and gravitational wave emission in neutron star mergers, Phys. Rev. D **91**, 124056 (2015).

[15] C. Helstrom, Minimum mean-squared error of estimates in quantum statistics, Phys. Lett. **25A**, 101 (1967).

[16] V. B. Braginsky, M. L. Gorodetsky, F. Y. Khalili, and K. S. Thorne, Energetic quantum limit in large-scale interferometers, AIP Conf. Proc. **523**, 180 (2000).

[17] M. Tsang, H. M. Wiseman, and C. M. Caves, Fundamental Quantum Limit to Waveform Estimation, Phys. Rev. Lett. **106**, 090401 (2011).

[18] S. L. Danilishin, F. Y. Khalili, and H. Miao, Advanced quantum techniques for future gravitational-wave detectors, Living Rev. Relativity **22**, 2 (2019).

[19] H. Miao, N. D. Smith, and M. Evans, Quantum Limit for Laser Interferometric Gravitational-Wave Detectors from Optical Dissipation, Phys. Rev. X **9**, 011053 (2019).

[20] K. Ackley, V. B. Adya, P. Agrawal, P. Altin, G. Ashton, M. Bailes, E. Baltinas, A. Barbuio, D. Beniwal, C. Blair *et al.*, Neutron star extreme matter observatory: A kilohertz-band gravitational-wave detector in the global network, Pub. Astron. Soc. Aust. **37**, e047 (2020).

[21] J. Eichholz, N. A. Holland, V. B. Adya, J. V. van Heijningen, R. L. Ward, B. J. J. Slagmolen, D. E. McClelland, and D. J. Ottaway, Practical test mass and suspension configuration for a cryogenic kilohertz gravitational wave detector, Phys. Rev. D **102**, 122003 (2020).

[22] D. Ganapathy, L. McCuller, J. G. Rollins, E. D. Hall, L. Barsotti, and M. Evans, Tuning Advanced LIGO to kilohertz signals from neutron-star collisions, Phys. Rev. D **103**, 022002 (2021).

[23] H. Miao, Y. Ma, C. Zhao, and Y. Chen, Enhancing the Bandwidth of Gravitational-Wave Detectors with Unstable Optomechanical Filters, Phys. Rev. Lett. **115**, 211104 (2015).

[24] M. A. Page, M. Goryachev, H. Miao, Y. Chen, Y. Ma, D. Mason, M. Rossi, C. D. Blair, L. Ju, D. G. Blair, A. Schliesser, M. E. Tobar, and C. Zhao, Gravitational wave detectors with broadband high frequency sensitivity, Commun. Phys. **4**, 27 (2021).

[25] T. Zhang, J. Bentley, and H. Miao, A broadband signal recycling scheme for approaching the quantum limit from optical losses, Galaxies **9**, 3 (2021).

[26] M. Korobko, Y. Ma, Y. Chen, and R. Schnabel, Quantum expander for gravitational-wave observatories, Light Sci. Appl. **8**, 118 (2019).

[27] S. Hild and A. Freise, A novel concept for increasing the peak sensitivity of LIGO by detuning the arm cavities, Classical Quantum Gravity **24**, 5453 (2007).

[28] S. H. Huttner, S. L. Danilishin, B. W. Barr, A. S. Bell, C. Grf, J. S. Hennig, S. Hild, E. A. Houston, S. S. Leavey, D. Pascucci, B. Sorazu, A. P. Spencer, S. Steinlechner, J. L. Wright, T. Zhang, and K. A. Strain, Candidates for a possible third-generation gravitational wave detector: Comparison of ring-sagnac and sloshing-sagnac speed-meter interferometers, Classical Quantum Gravity **34**, 024001 (2017).

[29] S. H. Huttner, S. L. Danilishin, S. Hild, and K. A. Strain, Comparison of different sloshing speedmeters, Classical Quantum Gravity **37**, 085022 (2020).

[30] A. Thüring, H. Lück, and K. Danzmann, Analysis of a four-mirror-cavity enhanced michelson interferometer, Phys. Rev. E **72**, 066615 (2005).

[31] P. Purdue and Y. Chen, Practical speed meter designs for quantum nondemolition gravitational-wave interferometers, Phys. Rev. D **66**, 122004 (2002).

[32] A. Freise, H. Miao, and D. D. Brown, Simplified optical configuration for a sloshing-speedmeter-enhanced gravitational wave detector, Classical Quantum Gravity **37**, 025007 (2020).

[33] J. Mizuno, K. Strain, P. Nelson, J. Chen, R. Schilling, A. Rdiger, W. Winkler, and K. Danzmann, Resonant sideband extraction: A new configuration for interferometric gravitational wave detectors, Phys. Lett. A **175**, 273 (1993).

[34] S. L. Danilishin, C. Gräf, S. S. Leavey, J. Hennig, E. A. Houston, D. Pascucci, S. Steinlechner, J. Wright, and S. Hild, Quantum noise of non-ideal Sagnac speed meter interferometer with asymmetries, New J. Phys. **17**, 043031 (2015).

[35] T. Zhang *et al.*, Quantum noise cancellation in asymmetric speed metres with balanced homodyne readout, New J. Phys. **20**, 103040 (2018).

[36] A. Freise, G. Heinzel, H. Lck, R. Schilling, B. Willke, and K. Danzmann, Frequency-domain interferometer simulation with higher-order spatial modes, Classical Quantum Gravity **21**, S1067 (2004).

[37] K. Komori, D. Ganapathy, C. Whittle, L. McCuller, L. Barsotti, N. Mavalvala, and M. Evans, Demonstration of an amplitude filter cavity at gravitational-wave frequencies, Phys. Rev. D **102**, 102003 (2020).

[38] L. Barsotti, L. McCuller, M. Evans, and P. Fritschel, The a+ design curve, LIGO Document T1800042, 2018.

[39] H. Miao, H. Yang, and D. Martynov, Towards the design of gravitational-wave detectors for probing neutron-star physics, Phys. Rev. D **98**, 044044 (2018).

[40] A. F. Brooks *et al.*, Overview of Advanced LIGO adaptive optics, Appl. Opt. **55**, 8256 (2016).

[41] J. R. Sanders and S. W. Ballmer, Folding gravitational-wave interferometers, Classical Quantum Gravity **34**, 025003 (2017).